Flapless Aircraft Control Via Curved Surface Jet Blowing

M Berati Kilic[1*], **Arzu Ismi**[4], **M Emre Cetin**[1], **Ismail Bayraktar**[1], **Yusuf Erdinc**[4], **Safa Dumanli**[3] **and Oguzhan Murat**[2]

[1]Department of Aeronautics and Astronautics Engineering, Istanbul Technical University, Istanbul, Türkiye

[2]Department of Aerospace Engineering, Ankara Yildirim Beyazit University, Ankara, Türkiye

[3]Turkish Aerospace Industries, Ankara, Türkiye

[4]Independent Researcher, Türkiye

E-mail: mberati@outlook.com

Abstract. This study investigates a novel flapless aircraft control system using curved wing surfaces with linear jet outlets for active flow control (AFC). Inspired by platforms like DARPA X-65 and MAGMATECH Xplore, the system injects high-momentum air to alter pressure distribution and generate control forces that eliminate the need for mechanical flaps or ailerons. This approach reduces drag, improves efficiency, enhances reliability, and allows for greater maneuverability. The research includes a 2D validation on a NACA 4416 airfoil and a 3D simulation using a B-2-inspired wing, demonstrating the feasibility of jet blowing as an alternative flight control method.

1 Introduction

In recent years, the aerospace industry has explored alternative methods of flight control that avoid the use of conventional hinged surfaces such as flaps and ailerons [1]. The motivation behind this effort lies in the potential benefits: reducing structural complexity and maintenance needs and increasing overall aerodynamic efficiency. Conventional high-lift devices, such as mechanical flaps, have limited deflection angles, which not only limit the aircraft's ability to maneuver abruptly but also cause structural inefficiencies due to mechanical linkages and hinge moments concentrated at the trailing edges.

A promising alternative to traditional hinged control surfaces lies in the field of active flow control (AFC). Among these, jet blowing techniques [2], which involve injecting high-momentum air into the boundary layer, are gaining increasing attention due to their ability to control lift, roll, and pitching forces without altering the external geometry of the aircraft. In such systems, the pressure distribution over the wing surface is actively manipulated by directing the jet flow, and the resulting aerodynamic forces can be controlled in real time by adjusting the mass flow rate of the injected air.

Various implementations of AFC exist, each differing in how and where the jet flow is introduced. A common strategy involves blowing air over a curved trailing edge surface, which redirects the flow in a controlled manner and modifies the pressure distribution on the wing. This configuration has been demonstrated in experimental UAV platforms such as the UK's MAGMA UAV [3] and the Demon [1] demonstrator from the FLAVIIR program by BAE Systems. In both cases, the curved surface integrated near the trailing edge of the wing features embedded slots through which air is expelled, enabling force generation comparable to mechanical flaps.

In contrast, the DARPA X-65 CRANE [4] project adopts a different approach. Rather than employing any curved trailing surface, the X-65 incorporates distributed blowing through embedded micro channels directly on the flat wing surface. These discrete channels modulate the boundary layer by locally injecting air through apertures, achieving aerodynamic control without altering the airframe's external geometry.

These diverse configurations underline the adaptability and innovation within AFC research. Whether through trailing-edge-integrated blowing surfaces as seen in MAGMA and Demon, or surface-embedded microjet arrays as in X-65, modern fluidic control systems are redefining the possibilities of maneuvering flight, eliminating the need for flaps and ailerons while maintaining or even improving aerodynamic performance.

This study aims to develop and analyze a flapless control mechanism using elliptically curved surfaces for AFC to achieve high maneuverability and aerodynamic performance without mechanical flaps.

2 Methodology

This study aims to develop a flapless control mechanism for aircraft by employing air blowing through specially designed surfaces, targeting the achievement of aerodynamic performance comparable to conventional flap-based systems. The approach utilizes elliptical curved surfaces for active flow control (AFC).

The study is divided into two main phases. In the first phase, two-dimensional aerodynamic analyses were conducted on the NACA 4416 airfoil to evaluate the effectiveness of the proposed method using a simplified configuration. During this phase, key performance parameters such as pressure distribution and lift coefficient were optimized based on the shape and position of the curved surfaces. This allowed for both validation of the methodology and identification of fundamental design parameters.

In the second phase, the findings from the two-dimensional analysis were used as a foundation for further investigation on a three-dimensional geometry inspired by the B-2 Spirit aircraft [5]. This step aimed to assess the applicability of the method in a more complex and realistic scenario, and to explore the aerodynamic benefits of curved surfaces in advanced platforms such as UAVs.

For both phases of the study, mesh generation was carried out using ANSYS ICEM CFD, while the flow simulations were conducted using ANSYS Fluent 2020 R2[6]. A consistent meshing methodology was adopted across different geometric configurations to ensure the reliability and comparability of the results.

2.1 2D Numerical Analysis: Methodology and Validation

2.1.1 Baseline Configuration: A baseline case with a NACA 4416 airfoil was selected for validation purposes. The configuration of the NACA 4416 airfoil is shown in Figure 1. Validation was performed for the baseline configuration at 0° angle of attack and 0° flap deflection [7].

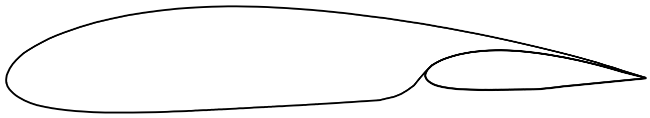

Figure 1: NACA 4416 Airfoil Configuration

The computational domain was generated using an unstructured mesh around the NACA 4416 airfoil. The computational domain used in the simulations is shown in Figure 2. The farfield boundaries were located at a distance of approximately 20 times the chord length c from the airfoil surface in all directions, as recommended in the literature[8, 9]. This choice ensures that boundary-induced effects are minimized, and that accurate prediction of lift and drag forces is maintained.

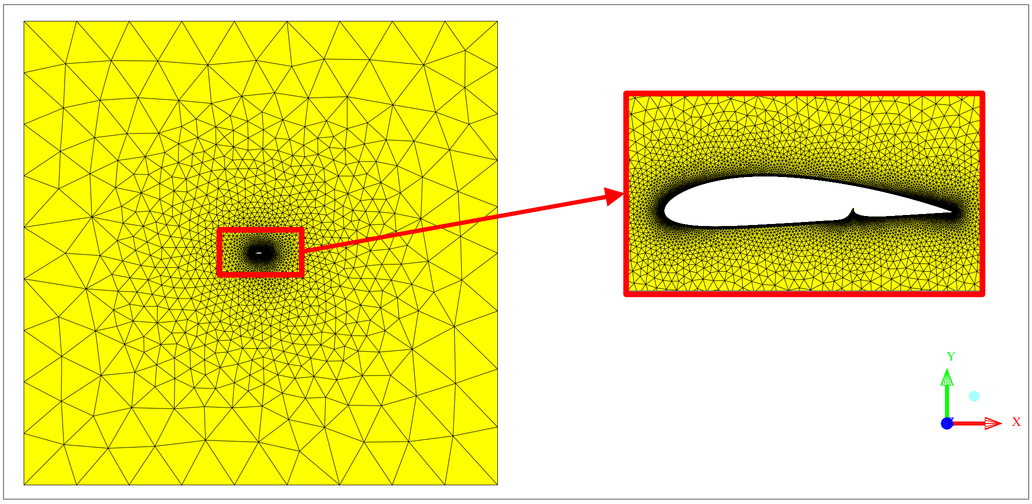

Figure 2: Schematic of the 2D Computational Domain and Mesh Used for the NACA 4416 Airfoil.

The following boundary conditions were applied in the 2D simulations:

- **Farfield (Pressure Farfield):** A pressure farfield boundary condition was applied to define the freestream conditions. The incoming flow parameters are summarized in Table 1. Additionally, the Reynolds number was calculated based on the chord length, resulting in $Re = 1.21 \times 10^6$ for a chord length of $c = 0.6096$ m.
- **Airfoil Surface (Wall):** A no-slip wall boundary condition was applied on the airfoil surface. Near-wall flow resolution was ensured with a mesh that provided $y^+ < 1$ for compatibility with low Reynolds number turbulence modeling.

Table 1: Freestream and Geometric Parameters for 2D CFD Simulations of the NACA 4416 Airfoil

Parameter	**Value**
Chord Length (c)	0.6096 m
Mach Number (M_∞)	0.23
Reynolds Number (Re)	1.21×10^6
Freestream Static Pressure (P_∞)	1013250 Pa

2.1.2 Simulation Setup: The simulations were performed using a steady-state Reynolds-averaged Navier–Stokes (RANS) approach to solve the governing equations of incompressible turbulent flow. The RANS methodology, despite averaging out turbulent fluctuations, remains widely used in aerodynamic studies due to its computational efficiency and reasonable accuracy for steady external flows[10].

For spatial discretization, a second-order upwind scheme was employed for the convective terms to improve solution accuracy without introducing excessive numerical diffusion[11]. The pressure-velocity coupling was handled using the fully coupled scheme, which simultaneously solves momentum and continuity equations. This method enhances the convergence rate and numerical stability compared to traditional segregated methods such as SIMPLE, especially in high-speed or compressible flows[12].

In the 2D simulations, the k–ω Shear Stress Transport (SST) model was selected for its ability to accurately capture adverse pressure gradient and flow separation effects, particularly near the airfoil surface[13]. The model blends the advantages of k–ω in the near-wall region and k–ε in the freestream.

A low-Reynolds-number mesh was used to fully resolve the boundary layer, with a first cell height selected to achieve $y^+ < 1$, ensuring that the flow near the wall lies entirely within the viscous sublayer and avoiding the use of wall functions[12].

2.1.3 Validation of CFD Results: The comparison of the pressure distribution and aerodynamic coefficients with the test data validated the numerical setup. The comparison of the pressure coefficient (C_p) distribution is presented in Figure 3.

The comparison of lift, drag and moment coefficients with the experimental data and CFD simulation is presented in Table 2. These values are based on the NACA 4416 airfoil [7].

Table 2: Comparison of Lift, Drag, and Moment Coefficients for NACA 4416 Airfoil

Case	C_l	C_d	C_m
NACA 4416 Experimental	0.4496	–	-0.0949
NACA 4416 CFD Simulation	0.4556	0.0078	-0.0950

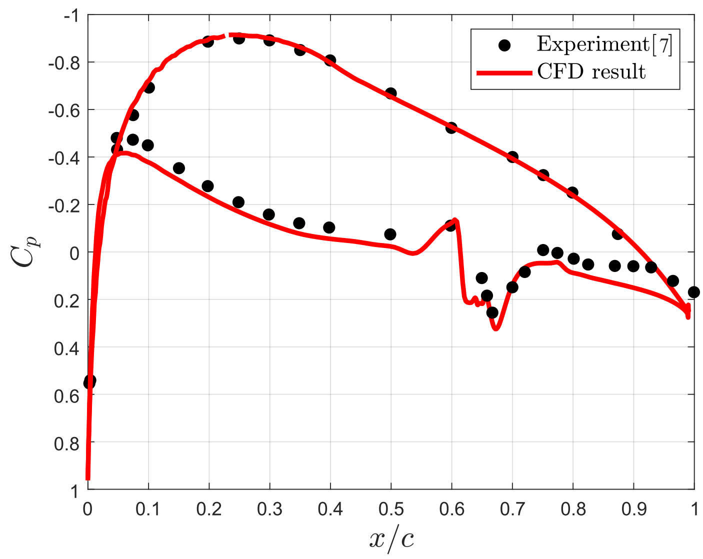

Figure 3: Comparison Between Experimental and CFD Results for the NACA 4416 Airfoil

To quantify the deviation between the experimental and simulated results, the relative errors are calculated and presented in Table 3. These values help assess the agreement between the CFD predictions and the reference data.

Table 3: Errors Between CFD and Experimental Data

Coefficient	**Error (%)**
C_l	1.343
C_d	–
C_m	0.095

As seen in Table 3, the relative errors between the CFD simulation and the experimental data are minimal, particularly for the lift and moment coefficients. The lift coefficient error is approximately 1.3%, and the moment coefficient error is almost negligible. Although the drag coefficient is unavailable for experimental comparison, the values obtained from the simulation remain within expected limits for airfoil flows at low angles of attack.

These results confirm the reliability of the CFD simulation in accurately capturing the aerodynamic behavior of the NACA 4416 airfoil. Therefore, it can be concluded that the numerical method and mesh configuration employed in the simulation are suitable for predicting aerodynamic characteristics with high confidence.

2.1.4 Curved Surface Configuration and Implementation: According to Buonanno[1], achieving a higher lift coefficient is favored when the slot height to thickness ratio (h/t) is minimized and the curved surface is positioned closer to the trailing edge, with optimal chordwise locations reported around 96–97%. In line with this, different chordwise positions (85%, 90%, and 95% of the chord length) were selected in this study to validate these findings by observing their influence on aerodynamic performance. The slot exit was defined along a straight line corresponding to 15%, 20%, and 25% of the local airfoil thickness for each configuration.

Additionally, Buonanno[1] suggests that for subsonic applications, a circular curved surface is preferred, whereas for transonic and supersonic regimes, an elliptical surface yields better performance. Since the targeted platforms for integration (ANKA-3 and KIZILELMA) are intended for operations in transonic and supersonic flight regimes, an elliptical curved surface was adopted. Although Buonanno[1] does not define a unique elliptical aspect ratio, this is consistent with the fact that circulation control performance is governed primarily by the effective local curvature of the curved surface rather than by a single geometric parameter. Accordingly, a semi-major to semi-minor axis ratio of 2:1 was selected in the present work to provide a moderate effective curvature, balancing jet turning capability and attachment robustness for high-speed blowing conditions. The technical drawing of the geometry, featuring a curved surface located at 95% of the chord and a slot height of 15% of the local thickness, is presented in Figure 4.

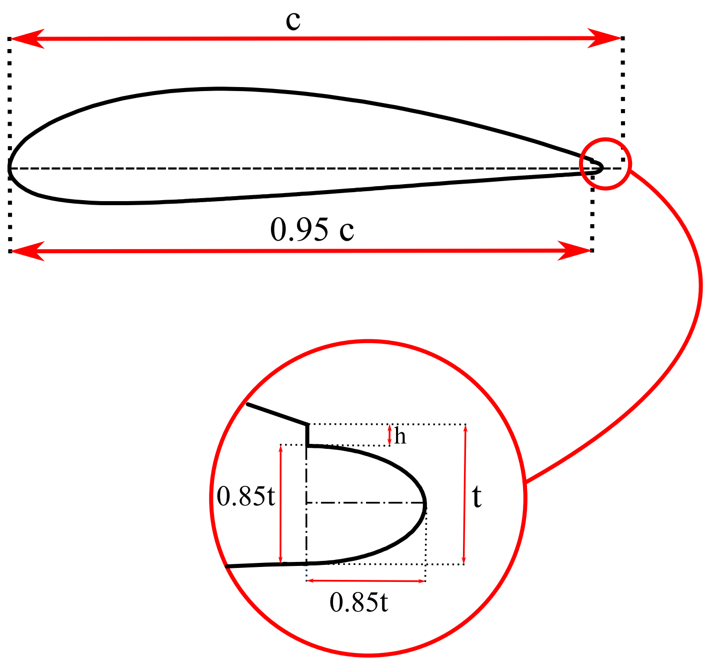

Figure 4: NACA 4416 With Blowing Surface

2.2 3D Numerical Study: Delta Wing and B-2 Inspired Wing

2.2.1 Turbulence Model Validation With 65° Delta Wing: For turbulence model validation, the boundary conditions were taken directly from [14], and the model configuration and geometry of NASA's 65° delta wing are presented in Table 4 and Figure 5, respectively.

Table 4: Freestream and Geometric Parameters for 3D CFD Simulations of NASA's 65° Delta Wing

Parameter	**Value**
Angle of attack (α)	5.2°
Mach Number (M_∞)	0.4
Reynolds Number (Re)	6.0×10^6
Freestream Static Pressure (P_∞)	165560.36 Pa

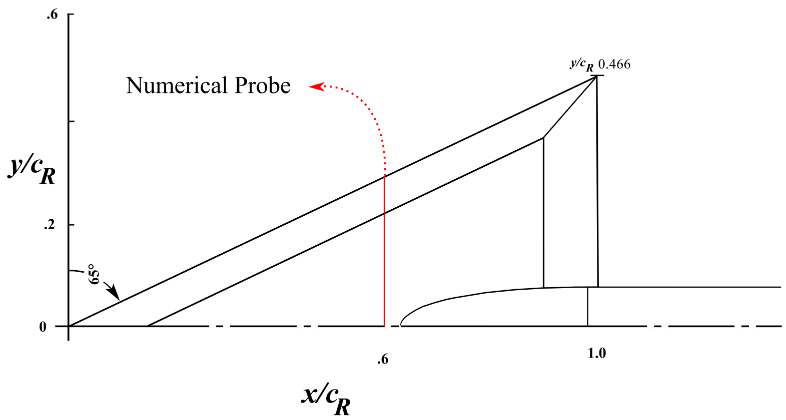

Figure 5: 65° Delta Wing Model

A symmetric computational domain was generated around the half-span geometry of NASA's 65-degree delta wing. To reduce computational cost, only half of the wing was modeled, and a symmetry plane was applied at the mid-span. The computational domain was spherical, with the outer boundaries located at a distance of approximately 20–25 times the mean aerodynamic chord from the geometry to minimize boundary interference[8, 9].

The following boundary conditions were applied:

- **Farfield (Pressure Farfield):** A pressure farfield boundary condition was imposed on the outer spherical domain to represent undisturbed freestream flow. The incoming flow parameters are summarized in Table 4.
- **Wing Surface:** A no-slip wall condition was applied to the wing surface to resolve the boundary layer.
- **Symmetry Plane:** A symmetry boundary condition was applied along the aircraft centerline to reduce computational cost while preserving the physical accuracy of the simulation.

The 3D CFD simulations were conducted using a steady-state RANS (Reynolds-averaged Navier–Stokes) approach, employing the realizable k–ε turbulence model due to its robustness in handling large-scale separation and swirling flows[15]. The realizable variant offers improved accuracy over the standard k–ε model, particularly for flows with strong curvature or rotation.

To ensure a good balance between accuracy and computational cost, scalable wall functions were applied with a near-wall resolution targeting $y^+ > 30$, placing the first cell within the logarithmic layer of the turbulent boundary layer[12]. This allowed coarser mesh near walls without significantly compromising accuracy.

The governing equations were discretized using a second-order upwind scheme for convective terms, which enhances numerical accuracy while controlling numerical diffusion[11]. A fully coupled solver was employed for pressure-velocity coupling, enabling simultaneous solution of continuity and momentum equations and improving numerical stability in complex aerodynamic flows.

The red line in Figure 5 indicates the location of the cross section where the pressure coefficient (C_p) distribution obtained from CFD results is compared with experimental data. The resulting simulation, compared against experimental surface pressure data in Figure 6, verified the model's ability to capture high-sweep-wing flows.

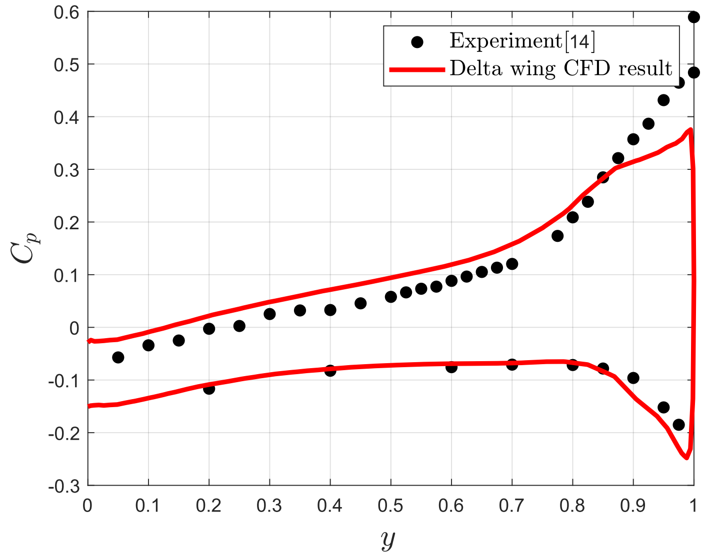

Figure 6: Pressure Coefficient Distribution at $x/C_R = 0.6$

2.2.2 Flapless B-2 Inspired Wing Simulations: Three-dimensional (3D) simulations were conducted on the B-2 Spirit-inspired wing geometry [5]. To ease the investigation, simplifications and scaling procedures, such as closing cavities in the reference geometry, were carried out. To ensure a consistent and systematic evaluation of aerodynamic performance, different geometric configurations were analyzed using a common meshing strategy.

Initially, a baseline configuration without flaps or a curved surface was simulated under boundary conditions adapted from NASA's "65 Degree Delta Wing" data. This configuration served as the reference for evaluating the effects of control surfaces.

Next, a flap-only configuration was created by introducing a 15° flap deflection. A new mesh was generated for this geometry using the same method as in the baseline case to ensure consistency. The simulations were repeated with identical flow conditions to observe the influence of flap deflection on aerodynamic coefficients.

In the final stage, the flap was replaced with a curved surface and a jet inlet, modeled following the approach used in earlier two-dimensional studies. A close-up view of the modified geometry is shown in Figure 7. The jet inlet was defined such that Mach number ratio was 2 ($M_{jet}/M_\infty = 2$).

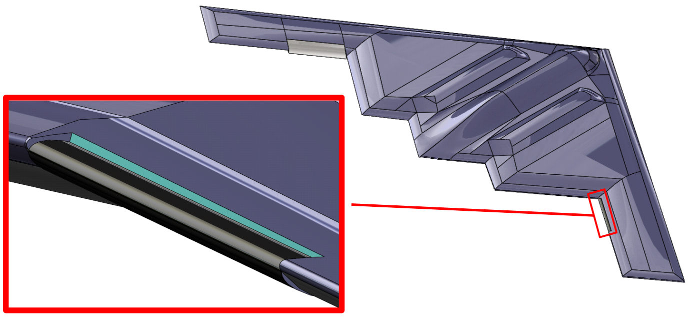

Figure 7: A Close-up View of the 3D Geometry of the B-2 Spirit

This systematic setup consisting of baseline, flap-only, and curved-surface-only configurations enabled a clear and isolated assessment of each design's aerodynamic contribution. Differences in lift coefficient (C_L) and moment coefficient (C_M), which was calculated about the quarter-chord point of the mean aerodynamic chord along the z-axis, were used to quantify the effectiveness of each modification relative to the baseline.

2.2.3 Mesh Independence Study: To ensure the reliability and consistency of the numerical results, a mesh independence study was systematically conducted. The study was not based on arbitrary mesh changes; rather, a systematic refinement and coarsening strategy was followed, within the limits of the available computational resources, to observe the convergence of aerodynamic coefficients. Table 5 shows the results obtained for the 15° flap deflection case at different mesh densities.

Table 5: Mesh Independence Study Results for 15° Flap Deflection Case

Mesh Density	**Element Count**	C_L	C_D	C_M
Coarse	4 M	0.0431	0.00494	-0.0189
Medium	5 M	0.0425	0.00489	-0.0186
Fine	5.9 M	0.0421	0.00486	-0.0184

Similarly, a mesh independence study was also carried out for the curved surface configuration. Table 6 shows the results obtained for the curved surface configuration at different mesh densities. It is observed that as the mesh is refined, the changes in the lift (C_L), drag (C_D), and moment (C_M) coefficients become negligible, indicating mesh independence. Based on these results, the medium mesh was selected for subsequent simulations. A close-up view of the medium mesh along the symmetry plane is shown in Figure 8.

Table 6: Mesh Independence Study Results for Curved Surface Configuration

Mesh Density	**Element Count**	C_L	C_D	C_M
Coarse	4.1 M	0.0491	0.0053	-0.0225
Medium	5.2 M	0.0514	0.0053	-0.0230
Fine	6.0 M	0.0512	0.0054	-0.0231

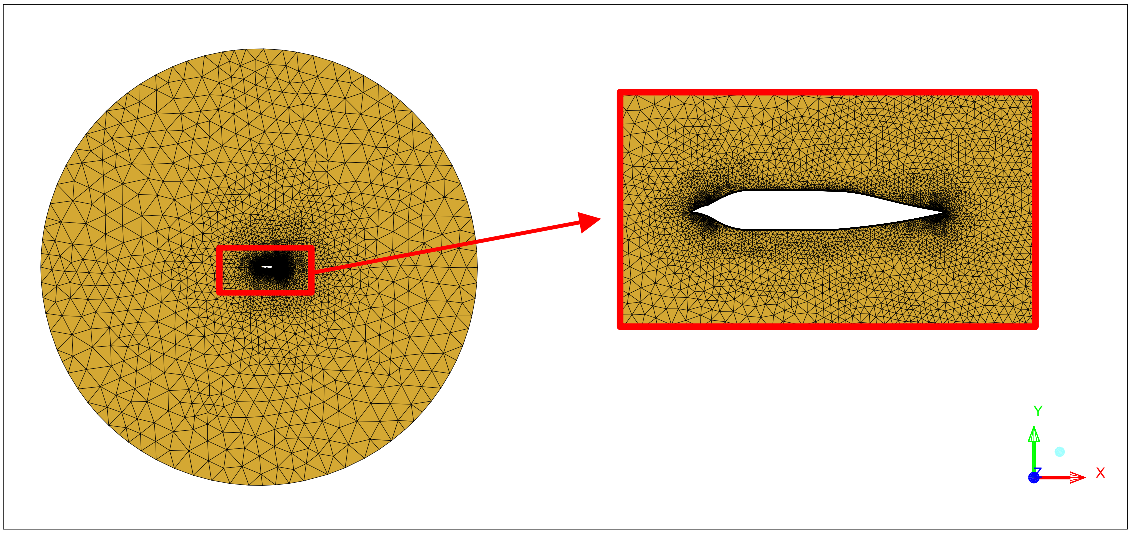

Figure 8: Close Up View of the Medium Mesh on the Symmetry Plane for the Curved Surface Configuration

3 Results and Discussion

3.1 Analysis of 2D Results

Following the methodology described in the related section, all geometries were created in accordance with the specified configurations and simulations were performed at the same mass flow rate. The results are presented in Table 7. In the initial stage, a jet blowing rate of 1.5 kg/s was selected in order to observe the changes in aerodynamic coefficients when the jet velocity approximately matched the free stream velocity. The same mass flow rate was used for all cases, as the objective was to isolate and analyze the effects of the position and height of the blowing surface and the curved surface on the flow behavior.

Table 7: Performance Metrics at Varying Blowing Configurations

Jet Blowing Rate (kg/s)	**Location**	**h/t**	C_l	C_d	C_m
1.5	**0.85c**	15%	0.13330	0.00919	-0.03531
		20%	0.14352	0.00956	-0.03717
		25%	0.14802	0.00971	-0.07500
	0.90c	15%	0.27051	0.00836	-0.05834
		20%	0.24980	0.00863	-0.05447
		25%	0.36683	0.00804	-0.07661
	0.95c	15%	0.42790	0.00827	-0.08973
		20%	0.37833	0.00803	-0.07910
		25%	0.36251	0.00797	-0.07564

As a result of the conducted analyses, the configuration with the curved surface located at 95% chord and a slot height of 15% thickness produced the highest increase in the lift coefficient, thereby supporting the conclusions reported by Buonanno [1]. The lift (C_l) and drag (C_d) coefficients obtained for the 95-15 configuration at different mass flow rates (i.e., M_{jet}/M_∞ ratios) are presented in Table 8.

Table 8: Aerodynamic Properties for Different Mass Flow Rates

Jet Blowing Rate (kg/s)	M_{jet}/M_∞	C_l	C_d	C_l/C_d
0.00	0.0000	0.3607	0.0087	41.4598
1.50	0.9065	0.4469	0.0081	55.4341
2.00	1.2087	0.5044	0.0085	59.6023
2.50	1.5109	0.5696	0.0091	62.8905
3.00	1.8131	0.6401	0.0098	65.5202
3.31	2.0000	0.6859	0.0103	66.8398
3.50	2.1153	0.7164	0.0106	67.7459
3.75	2.2663	0.7558	0.0111	68.3908
4.00	2.4174	0.7953	0.0116	68.7954
4.25	2.5685	0.8356	0.0121	69.1637
4.50	2.7196	0.8751	0.0127	69.1668
4.60	2.7801	0.8891	0.0129	68.7979
4.80	2.9009	0.9230	0.0134	68.8582
5.00	3.0218	0.9384	0.0142	66.0440
5.11	3.0892	0.9564	0.0144	66.3042
5.20	3.1427	0.9691	0.0147	66.1185
5.29	3.1976	0.9830	0.0149	66.0360
5.40	3.2635	0.9998	0.0152	65.9437
5.50	3.3240	1.0149	0.0154	65.8736

The variation of the C_l/C_d ratio for the 95-15 configuration under different jet inlet conditions is presented in Figure 9.

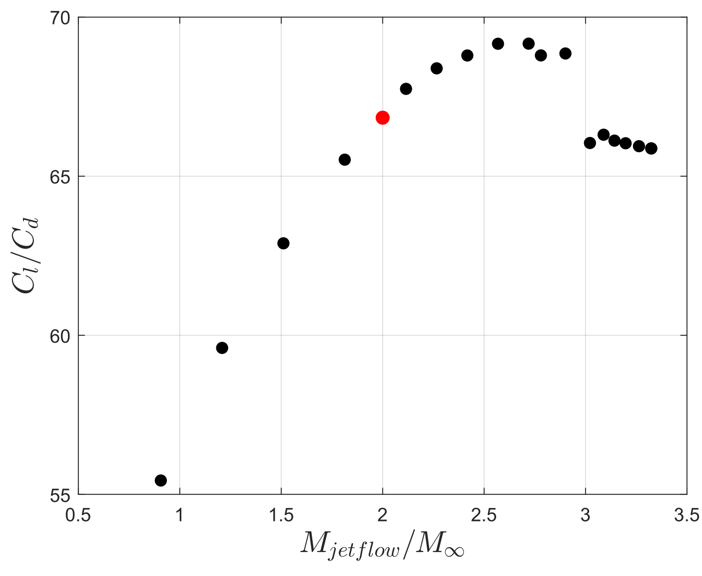

Figure 9: Variation of C_l/C_d With M_{jet}/M_∞ for the 95-15 Configuration

By referring to Figure 9, the relationship between the Mach number of the jet flow on an elliptical curved surface and its performance (C_l/C_d) relative to the freestream Mach number has been examined. The results obtained show that the C_l/C_d ratio initially increases as the Mach number of the jet flow relative to the freestream increases, but decreases significantly beyond a certain Mach ratio. This indicates that as the velocity of the jet flow increases, the flow becomes more complex and approaches the transonic region, leading to a reduction in aerodynamic efficiency. Particularly at high Mach numbers, factors such as shock waves and compression losses have been observed to increase drag, negatively affecting performance.

However, at intermediate Mach number ratios (around 2), the C_l/C_d ratio reaches its highest values, indicating that the jet flow operates more efficiently at this speed. The aerodynamic coefficients corresponding to the selected value shown in the figure are presented in Table 9. This finding emphasizes that the speed of the jet flow is a critical parameter for both lift production and flow efficiency.

In conclusion, it has been found that maintaining the Mach number of the jet flow at a certain level higher than the freestream is crucial for achieving high lift efficiency. However, exceeding a certain Mach number leads to a decline in performance and a reduction in efficiency.

Table 9: Aerodynamic Coefficients Corresponding to the Selected Point ($M_{jet}/M_\infty = 2$)

C_l	C_d	C_l/C_d	C_m
0.6859	0.0103	66.8398	-0.1448

Table 10: Effect of Jet Blowing Mach Ratio on Lift (C_l), Moment (C_m), and Lift to Drag Ratio (C_l/C_d) Coefficients

Parameter	$M_{jet}/M_\infty = 0.0$	$M_{jet}/M_\infty = 2.0$	**Increase**
C_l	0.3607	0.6859	×1.90
C_m	-0.0750	-0.1448	×1.93
C_l/C_d	41.4598	66.8398	×1.61

Table 10 compares the aerodynamic coefficients for the jet blowing application cases with Mach ratios of 0.0 and 2.0. In particular, with the application of jet blowing, the lift coefficient (C_l) has increased by approximately 1.90 times. Similarly, the absolute value of the pitching moment coefficient (C_m) has increased by approximately 1.93 times, indicating a stronger nose-down moment. Moreover, the lift to drag ratio (C_l/C_d) has increased by about 1.61 times, demonstrating a significant enhancement in aerodynamic efficiency due to jet blowing over an elliptical curved surface.

In this study, the moment reference point for the 2D airfoil case was selected as the quarter-chord location, since it is close to the aerodynamic center. Therefore, the variation in pitching moment with angle of attack remained very small.

According to the analysis results, the moment coefficient (C_m) values obtained for the curved-surface jet-blowing configuration were negative throughout the investigated range. As shown in Table 11, the airfoil section generated a nose-down pitching moment under jet blowing. For the baseline case, C_m values were approximately -0.095, whereas with jet blowing the values shifted to nearly -0.145. This shows that the jet-blowing application increased the nose-down pitching moment of the airfoil section.

Table 11: Moment Coefficient (C_m) With Angle of Attack for the Jet Blowing Configuration

AoA (°)	C_m $(M_{\text{jet}}/M_\infty = 2.0)$
-4	-0.1435
-2	-0.1442
0	-0.1448
2	-0.1454
4	-0.1455

As seen in Table 11, the moment coefficient at the quarter-chord remained almost constant with angle of attack, with only a slight and nearly linear decrease. This suggests that the aerodynamic-center characteristics of the airfoil section were not significantly altered by jet blowing. Therefore, within the examined angle-of-attack range, the jet-blowing configuration did not indicate any adverse effect on the static stability characteristics of the 2D airfoil section.

3.2 Results of 3D Simulations

3.2.1 Flow Field Visualization: To better understand the aerodynamic behavior, flow field contour plots were generated. These visualizations highlight the differences in flow behavior around the surface of the wing in different configurations.

Figure 10 illustrates the pressure distributions over mid plane of the curved surface and how the jet flow dramatically alters the aerodynamic performance. The contour on the left (Figure 10(a)) represents the case without jet flow ($M_{jet} = 0.0$). In this scenario, the pressure distribution across the surface is relatively uniform, with no significant low pressure region apparent.

In contrast, the contour on the right (Figure 10(b)) shows the pressure distribution when the jet flow is applied ($M_{jet} = 0.8$). A striking feature is the development of a substantial low pressure area, indicated by the bright blue and green hues, immediately above the region where the jet is blown. This low pressure zone is a direct consequence of the elliptical surface, where the blown jet adheres to the surface, deflects the flow downwards, and generates a suction effect, thus reducing the pressure on the surface.

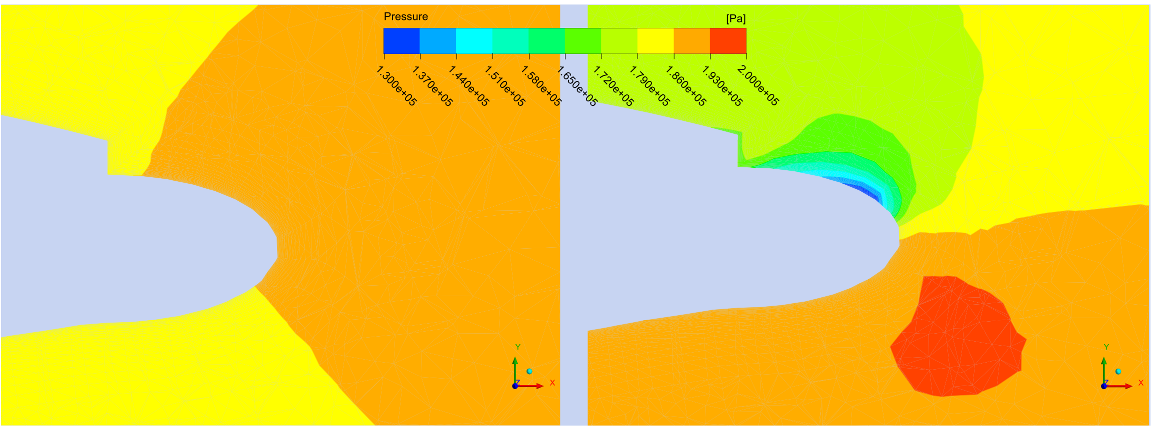

(a) Jet Flow $M_{jet}/M_{\infty} = 0$ (b) Jet Flow $M_{jet}/M_{\infty} = 2$

Figure 10: Pressure Distribution Over Mid Plane of the Curved Surface

This alteration in the pressure field, as visualized in the contours, directly correlates with the significant changes observed in the aerodynamic coefficients presented in Table 12. The intense low pressure region created by the jet flow is responsible for the considerable increase in the lift coefficient (C_L). The lower pressure on the upper surface results in a greater net upward force on the airfoil, leading to a much higher C_L value. As seen in the table, C_L at $M_{jet} = 0.8$ increases by approximately five times compared to the no jet flow condition.

Simultaneously, this modification in the pressure distribution also influences the moment coefficient (C_M). The low pressure area, particularly towards the trailing edge of the surface, contributes to an increased nose down pitching moment. The larger absolute value of the negative C_M in Table 12 for $M_{jet} = 0.8$ confirms this effect.

From a performance perspective, the pressure manipulation achieved through the jet flow leads to a remarkable improvement in the lift to drag ratio (C_L/C_D). The high lift force generated by the pronounced low pressure region in Figure 11 translates to an approximately 3.7 times increase in the C_L/C_D ratio in Table 12. This enhancement signifies that significantly more lift is produced for the same amount of drag, which is a crucial indicator of aerodynamic efficiency. Such an improvement can yield benefits in fuel efficiency, range, and maneuverability, all critical flight parameters.

Table 12: Aerodynamic Coefficients at Different Mach Numbers of Jet Flow Over Elliptical Surface

Jet Flow Mach Ratio ($M_{\text{jet}}/M_{\infty}$)	0.0	2
C_L	0.0098	0.0514
C_D	0.0037	0.0053
C_M	-0.0073	-0.0230
C_L/C_D	2.6414	9.7836

In this section, the wake pressure distribution downstream of the curved surface is examined. Figure 11 shows the definition of the custom cutting plane used for this analysis. The cutting plane is adapted to the wing geometry, oriented parallel to the jet blowing surface, and positioned within the wake region to enable clearer observation of the flow alterations induced by jet actuation.

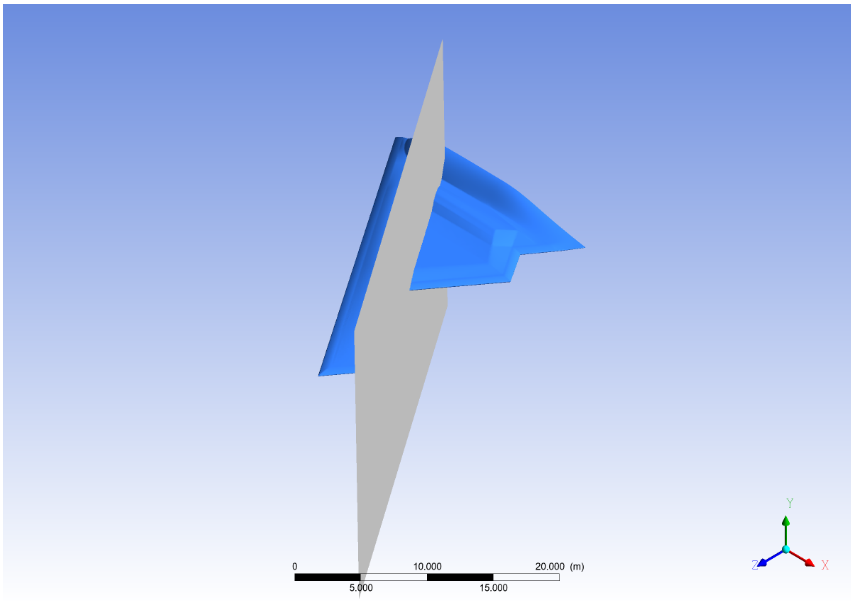

Figure 11: Definition of the Custom Cutting Plane Used for Wake Pressure Visualization

Figure 12 presents the wake pressure distribution for two different jet flow conditions. Figure 12(a) shows the baseline case without jet actuation ($M_{\text{jet}} = 0.0$). In this scenario, a symmetric and wider low pressure region is observed in the wake, which indicates greater drag. Without jet blowing, the flow naturally separates from the surface without adhering to the curved surface contour, resulting in a conventional wake structure.

In contrast, Figure 12(b) shows the case with a high speed jet ($M_{\text{jet}} = 0.8$), where the wake pressure distribution is significantly altered. Due to the jet blowing, the flow adheres to the curved surface and is deflected, causing a notable reduction in the low pressure wake region. This leads to an increase in base pressure and a corresponding decrease in drag. Furthermore, the asymmetric pressure distribution induced by the jet demonstrates that the curved surface effectively generates a control force by deflecting the flow.

In conclusion, jet blowing over an elliptical surface positively alters the wake pressure field by reducing drag and enhancing the potential for aerodynamic control.

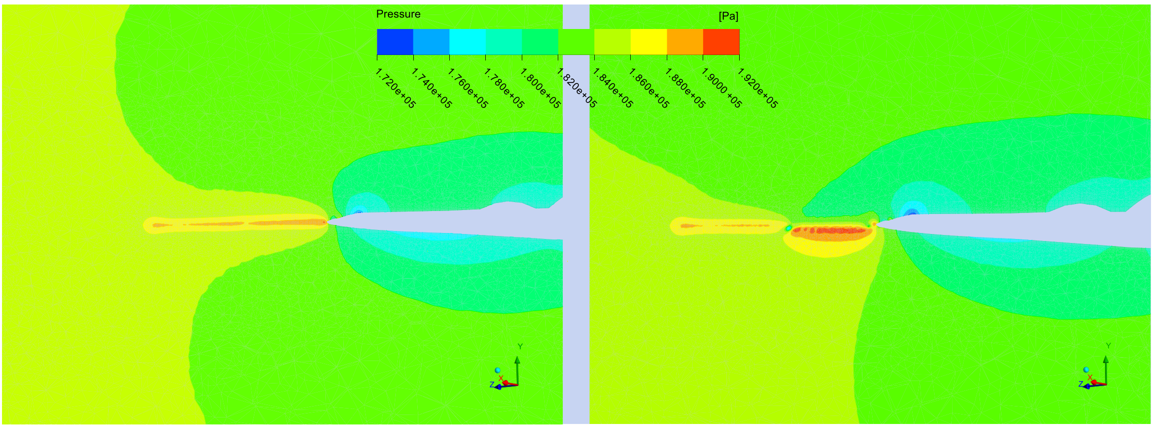

(a) Jet Flow $M_{jet}/M_{\infty} = 0$ (b) Jet Flow $M_{jet}/M_{\infty} = 2$

Figure 12: Wake Pressure Distribution Downstream of the Curved Surface

3.2.2 Comparison of Aerodynamic Coefficients Although sufficient results had already been obtained with jet blowing at twice the freestream velocity, an additional simulation was conducted, for completeness, at a jet blowing ratio that yields the same C_L ($M_{jet}/M_{\infty} = 1.56$). Based on these data, the effectiveness of jet blowing over an elliptical curved surface was examined. The effectiveness was assessed by comparing the aerodynamic coefficients of three different configurations: no flap deflection, 15° flap deflection, and the curved surface configuration. As summarized in Table 13, the curved surface configuration has a lower drag coefficient while maintaining the same lift coefficient, resulting in the highest lift-to-drag ratio (C_L/C_D), demonstrating its superior aerodynamic performance.

Table 13: Comparison of the Aerodynamic Coefficients for Different Control Configurations

Parameter	No Flap Deflection	15° Flap Deflection	Elliptical Surface ($M_{jet}/M_{\infty} = 1.56$)
C_L	0.0110	0.0425	0.0425
C_D	0.0040	0.0049	0.0045
C_M	-0.0079	-0.0186	-0.0194
C_L/C_D	2.7763	8.6912	9.4444

Table 13 demonstrates that the curved surface configuration exhibits a lift generation capability comparable to that of the 15° flap deflection configuration, while operating with a lower drag coefficient. Therefore, when evaluated in terms of the C_L/C_D ratio, it is concluded that the curved surface configuration enhances aerodynamic efficiency.

4 Conclusion

The curved surface configuration is observed to generate moment coefficients of greater magnitude (C_M) compared to the conventional flap case. This suggests that the influence of the curved surface is not limited to lift and drag contributions, but may also have important implications for the longitudinal stability of the lifting system. Through active flow control, moments comparable in magnitude to those produced by conventional moving surfaces can be achieved solely by jet blowing along the surface. This presents a considerable advantage in modern aircraft designs, where requirements such as low radar cross section, ease of maintenance, and preservation of aerodynamic integrity are critical.

In summary, this study has demonstrated the feasibility of jet blowing over elliptical curved surfaces for flapless aircraft control. Both 2D and 3D simulations have shown promising results, particularly in terms of achieving or even surpassing the lift coefficient performance of traditional flap configurations. Further research could investigate the transient behavior and control authority under dynamic flight conditions.

Acknowledgments

This project was supported by the *Lift Up* program of Turkish Aerospace Industries (TUSAŞ) (project number: 66617995024d5). The authors also acknowledge the financial support provided by The Scientific and Technological Research Council of Türkiye (TUBITAK) under the 2209-B University-Industry Cooperation Support Program (Application number: 1139B412401878). During the course of this study, M Berati Kilic, Arzu Ismi, M Emre Cetin, Ismail Bayraktar and Yusuf Erdinc were affiliated with the Department of Aerospace Engineering, Ankara Yildirim Beyazit University, as undergraduate students. The authors used OpenAI's GPT-5.4 solely for English grammar, spelling, and language editing. The tool was not used to generate the scientific content, analysis, results, or conclusions of this work. All scientific content was produced, reviewed, and approved by the authors, who take full responsibility for the content of this article.

References

[1] Buonanno A 2009 *Aerodynamic circulation control for flapless flight control of an unmanned air vehicle* PhD Thesis Cranfield University, School of Engineering, Cranfield, UK

[2] Gupta S, Kumar S and Kumar R 2023 Effect on the aerodynamic characteristics of the delta wing using active flow control technique *14th Int. Conf. on Mechanical and Aerospace Engineering* (Portugal) pp 389–394 (doi:10.1109/ICMAE59650.2023.10424572)

[3] Owano N 2017 *MAGMA: work on flapless flight is taking off with initial flight trial success* Tech Xplore [online] Available at: https://techxplore.com/news/2017-12-magma-flapless-flight-trial-success.html (accessed 10 December 2024)

[4] Hitchens T 2023 *DARPA taps Aurora Flight Sciences for CRANE X-Plane design* Breaking Defense [online] Available at: https://breakingdefense.com/2023/01/darpa-taps-aurora-flight-sciences-for-crane-x-plane-design/ (accessed 10 December 2024)

[5] Taqiyuddin Z 2024 *B2-Spirit* GrabCAD Library, Model AU30 M01V1 X.SLDPRT [online] Available at: https://grabcad.com/library/b2-spirit-30 (accessed 5 March 2025)

[6] ANSYS Inc. 2020 *ANSYS Fluent Theory Guide, Release 2020 R2* (Canonsburg, PA: ANSYS Inc.)

[7] Bingham G J and Noonan K W 1974 *Low speed aerodynamic characteristics of NACA 6716 and NACA 4416 airfoils with 35 percent-chord single-slotted flaps* NASA Technical Memorandum NASA-TM-X-2623 [online] Available at: https://ntrs.nasa.gov/citations/19740013521 (accessed 3 February 2025)

[8] Lee-Rausch E, Vatsa V and Rumsey C 2006 Computational analysis of dual radius circulation control airfoils *3rd AIAA Flow Control Conference* AIAA 2006-3012 (doi:10.2514/6.2006-3012)

[9] NASA Turbulence Modeling Resource 2022 *CFD best practice guidelines for airfoil simulations* NASA Langley Research Center, Hampton, VA [online] Available at: https://turbmodels.larc.nasa.gov (accessed 9 February 2025)

[10] Pope S B 2000 *Turbulent Flows* (Cambridge: Cambridge University Press) (doi:10.1017/CBO9780511840531)

[11] Ferziger J H and Perić M 2002 *Computational Methods for Fluid Dynamics* (Berlin: Springer) (doi:10.1007/978-3-642-56026-2)

[12] Versteeg H K and Malalasekera W 2007 *An Introduction to Computational Fluid Dynamics: The Finite Volume Method* 2nd edn (Harlow, UK: Pearson Education)

[13] Menter F R 1994 Two-equation eddy-viscosity turbulence models for engineering applications *AIAA J.* **32** 1598–1605 (doi:10.2514/3.12149)

[14] Chu J and Luckring J M 1996 *Experimental surface pressure data obtained on 65° delta wing across Reynolds number and Mach number ranges, volume 3: medium-radius leading edge* NASA Technical Memorandum 4645, vol 3, NASA Langley Research Center, Hampton, VA [online] Available at: https://ntrs.nasa.gov/archive/nasa/casi.ntrs.nasa.gov/19960020435.pdf (accessed 26 February 2025)

[15] Shih T-H, Liou W W, Shabbir A, Yang Z and Zhu J 1995 A new k–ε eddy viscosity model for high Reynolds number turbulent flows—model development and validation *Comput. Fluids* **24** 227–238 (doi:10.1016/0045-7930(94)00032-T)